Laser-Directed Energy Deposition of Ti-Mo Biomaterials: Influencing Mechanisms of Molybdenum on Microstructure and Performance

Increasing or decreasing the amount of Mo affected formation and cohesive energies, grain refining efficiency, and other factors

BY D. SHU, L. ZHAO, D. WU, Y. GUO, Z. ZHANG, AND N. MA

Abstract

Ti-Mo alloys with variable molybdenum (Mo) contents were fabricated by the laser-directed energy deposition process. The in-depth influencing mechanisms of the Mo element on microstructure and performance were quantitatively analyzed by experiment and first-principal calculation. Increasing Mo content decreased the formation and cohesive energies and stabilized the β phase. The grain refining efficiency was increased, and the relative grain size was decreased by increasing the Mo content. The M_s temperature decreased, and the acicular martensite formed with increasing Mo content. Both the solid-solution hardening and fine grain strengthening effects had positive influences, while the β phase softening effect had a negative influence on the hardness and wear performance with increasing Mo content.

Keywords

- Laser-Directed Energy Deposition Process
- Ti-Mo Alloy
- First-Principal Calculation
- Solid-Solution Hardening
- Fine Grain Strengthening

Introduction

Titanium alloys have been one of the most widely used implant materials owing to their high strength-to-weight ratio, high biocompatibility, and biocorrosion resistance (Ref. 1). However, the wear performance of conventional titanium alloys is relatively low, and their elastic modulus is

much higher than that of human bone (~30 GPa) (Ref. 2). The elastic modulus mismatch could cause a "stress-shielding" effect, thereby leading to bone resorption and implant failure (Ref. 3).

Ti-Mo alloys have been developed to decrease the elastic modulus. The Mo element is nontoxic and has significant influences on the phase morphology and performance of the Ti-Mo alloys. Cardoso et al. (Ref. 4) and the phase diagram showed that the β phase increased with increasing Mo content. Xie et al. (Ref. 5) suggested that the Ti-Mo alloys fabricated by selective laser sintering comprised dominant α and β phases, and the Mo element stabilized the β phase. As the elastic modulus and hardness of the Ti-Mo alloys are sensitive to the crystal structure and phase morphology, Zhang et al. (Ref. 6) and Cardoso et al. (Ref. 4) presented that Mo content affected the elastic modulus and hardness by changing the phase balance. Xu et al. (Ref. 7) also proposed that the compressive strength and bending strength of the Ti-Mo alloys decreased with increasing Mo content. However, the in-depth influencing mechanisms of the Mo element have not been fully considered to date.

Various manufacturing techniques have been employed to fabricate the Ti-Mo alloys, such as casting (Ref. 8), microwave sintering (Ref. 7), laser powder bed fusion processing (Ref. 9), and laser-directed energy deposition (L-DED) (Ref. 10). L-DED is one type of additive manufacturing process where a laser beam is used to form a molten pool in a solid metal substrate, into which a stream of blown powder is injected (Ref. 11). Compared with the former processes, L-DED could reliably and efficiently produce Ti-Mo components at a low cost. In this study, L-DED was employed to fabricate the Ti-Mo alloys with variable Mo contents. The phase morphology, microstructure, hardness, elastic modulus, and wear performance were investigated. A first-principal calculation of the Ti-Mo alloys was also carried out using density-functional theory (DFT). The influencing mechanisms of the Mo element on the microstructure and performance of the Ti-Mo alloys were revealed.
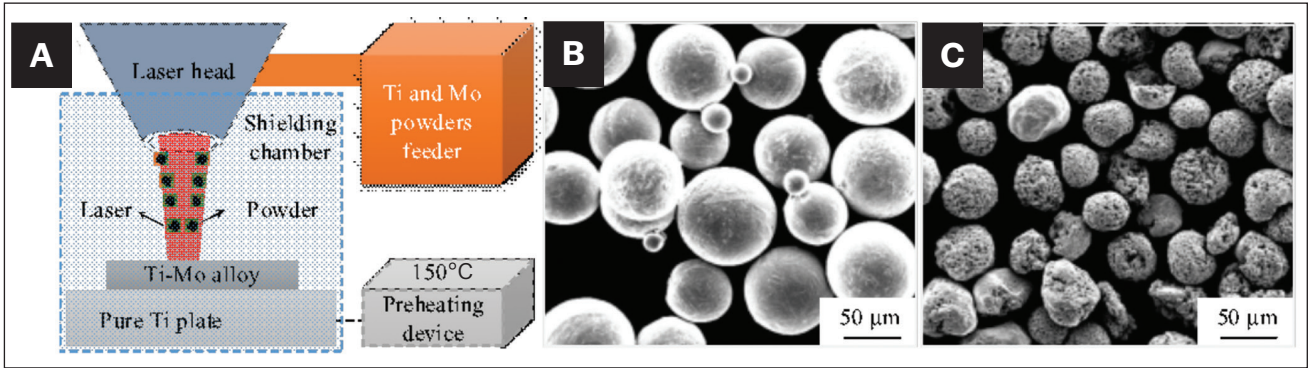
Fig. 1— A — Diagram of LMD of Ti-Mo alloys; B — surface morphology of pure Ti powders; C — surface morphology of pure Mo powders.

Experiment Procedures

Fig. 1A shows a diagram of L-DED of Ti-Mo alloys. Pure Ti plates with a dimension of 100 mm (3.93 in.) × 100 mm × 5 mm (0.197 in.) were used as the substrate. Gas-atomized pure Ti (purity > 99.4%) and Mo (purity > 99.6%) powders were adopted as the deposited materials, as shown in Figs. 1B and C. The powders were mechanically mixed using a ball milling machine (MITR-YXQM-4L) for 6 h with Al_2O_3 balls at a rotation speed of 400 r/min. During the milling, the mill was filled with pure Ar gas. Before the experiment, the powders were dried in a vacuum oven to eliminate moisture, and the substrates were preheated to 150°C (302°F) to suppress crack formation.

The commercial laser machine IPG YLS-6000 with a wavelength of 1080 nm and a spot diameter of 2.0 mm was adopted as the laser source. The laser power was 1.5 kW, and the scanning speed was 0.3 m (0.079 in.)/min. To control the oxygen content to be below 100 ppm, the shielding chamber was filled with pure Ar gas (99.99% purity) before L-DED, and the Ar gas flow rate of the powder nozzle was 9.2 L/min during L-DED. The overlapping ratio of the deposited tracks was 50%. Five multitrack and multilayer Ti-xMo alloy samples (x = 10 wt-% [Case 1], 15 wt-% [Case 2], 20 wt-% [Case 3], 25 wt-% [Case 4], 30 wt-% [Case 5] with average measured values of 9.5 wt-%, 15.6 wt-%, 19.0 wt-%, 25.4 wt-%, and 30.3 wt-%, respectively, and a dimension of 50 mm [1.968 in.] × 30 mm [1.181 in.] × 10 mm [0.394 in.]) were fabricated. The optical densities were obtained using the percentages of pores (e.g., 1-%pores), and the values were 99.58%, 99.63%, 99.07%, 98.38%, and 96.87%, respectively.

After the L-DED, for each Ti-xMo alloy sample, one specimen was obtained for microstructure analysis and three specimens were obtained for performance analyses. The metallographic specimens were prepared using the standard mechanical polishing method and etched with a Kroll solution (2.5% HNO_3 + 1% HF + 1.5% HCl + 95% H_2O) for 70 s. The phase compositions were identified by x-ray microdiffraction (XRD, Bruker D8 Advance), and the microstructural characterizations were investigated by scanning electron microscopy (SEM, EM30AXP). The hardnesses of the specimens were measured by a Vickers hardness tester (HV-1000Z) at a load of 300 g (0.661 lb) and a dwell time of 6 s. The average hardnesses of five measurements were

presented. Nanoindentation tests were performed on the specimens using a Hysitron TriboIndenter system equipped with a Berkovich indenter. The indents were made using an applied load of 200 mN, a loading rate of 600 mN/min, and a dwell time of 5 s. Dry sliding wear tests were evaluated using a ball-on-disc-type wear tester (MRH-5000W) at a test load of 40 N, a sliding speed of 500 r/min, a friction radius of 6 mm (0.236 in.), and a test time of 900 s. The coefficient of friction (COF) after reaching steady state was calculated by:

$$COF = F/N \tag{1}$$

where F is the friction force and N is the normal force.

First Principal Model

The geometry optimization, elastic, and electronic properties of Ti-xMo alloys are predicted based on the density functional theory (Ref. 12). The projector-augmented wave method is utilized to deal with ion-electron interactions. The generalized gradient approximation is employed to describe exchange and correlation function (Ref. 13). A body-centered cubic (bcc) structure is used to model the bcc β-Ti phase. The metallurgical tendency to form a solid solution depends on the formation energy (E_f). The cohesive energy (E_c) is defined as the work that is needed when a crystal decomposes into single atoms. E_f and E_x can be calculated by (Ref. 14):

$$E_f = \frac{1}{N_{total}}(E_{total} - N_{Ti}E_{solid}^{Ti} - N_{Mo}E_{solid}^{Mo}) \tag{2}$$

$$E_c = \frac{1}{N_{total}}(E_{total} - N_{Ti}E_{Ti}^{atom} - N_{Mo}E_{Mo}^{atom}) \tag{3}$$

where N_{total}, N_{Ti}, N_{MO} are the numbers of total atoms, Ti atoms and Mo atoms, respectively, E_{total} is the total energy of the cell, E_{solid}^{Ti} and E_{solid}^{Mo} are the energies of Ti and Mo atoms with
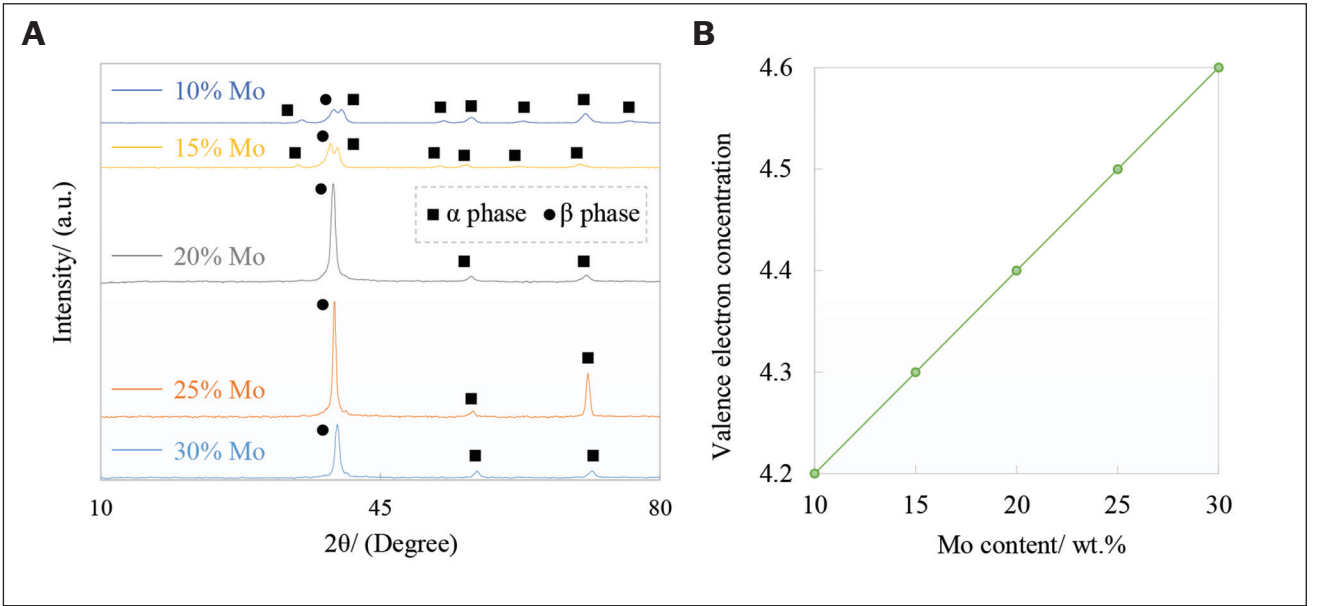
Fig. 2 — A — XRD patterns of the Ti-xMo alloys; B — valence electron concentration.

equilibrium lattice parameters, respectively, and E_{Ti}^{atom} and E_{Mo}^{atom} are the energies of isolated Ti and Mo atoms, respectively.

For a bcc lattice, there are three independent elastic constants: C_{11}, C_{12}, C_{44}. The bulk modulus B, shear modulus G, and Young's modulus E can be calculated by the elastic constants based on the Voigt-Reuss-Hill method (Ref. 15):

$$E = 9BG/(3B + G) \tag{4}$$

$$B = 1/2(B_V + B_R) \tag{5}$$

$$G = 1/2(G_V + G_R) \tag{6}$$

where B_V and G_V are the bulk modulus and shear modulus, respectively, calculated by the Voigt approximation method, and B_R and G_R are the bulk modulus and shear modulus, respectively, calculated by the Reuss approximation method.

The microhardness of isotropic solids is calculated by (Ref. 16):

$$H_v = (1 - 2\sigma)E/[6(1 + \sigma)] \tag{7}$$

where σ is the Poisson's ratio.

Results

The XRD patterns of the Ti-xMo alloys are shown in Fig. 2A. All the Ti-xMo alloys contained hcp α-Ti and bcc β-Ti phases. When the Mo content was 10 wt-%, the intensities of the α and β peaks were comparable. With increasing Mo content, the intensity of the β peak became stronger. The β phase became the dominant phase when the Mo content increased to 20 wt-% or a higher value. Previous studies suggested that an average electron-atom ratio of 4.2 (Pauling valence) was required for stabilizing the β phase in quenched titanium alloys (Ref. 17). The calculated valence electron concentrations of the Ti-xMo alloys are presented in Fig. 2B, and all the values are equal to or higher than 4.2, showing the high stability of the β phase.

As shown in Fig. 3A, the microstructure of the Ti-10 wt-% Mo alloy consisted of equiaxed matrix grains (prior β phase) and lath martensites (M); the grain size was as high as 197.8 μm. With increasing Mo content, the size of the equiaxed grains decreased. In addition, the coarse lath martensites changed to fine acicular martensites, as presented in Figs. 3B-E. Acicular martensite exhibited a needle-like morphology, forming elongated, interwoven structures within the matrix. In contrast, lath martensites tended to have a flat, layered appearance, often forming in grouped packets with distinct orientations (Ref. 18).

The measured hardnesses of the Ti-xMo alloys are shown in Fig. 3F. The average hardness increased with increasing Mo content, except for the Ti-30 wt-% Mo alloy. The peak hardness (481.3 HV) was observed for 25 wt-% Mo.

The *COF* values of the Ti-xMo alloys are shown in Fig. 4A. The *COF* value decreased with increasing Mo content, except for the Ti-30 wt-% Mo alloy. The minimum *COF* value was observed for 25 wt-% Mo. As shown in Fig. 4B, debris was accumulated, and some peeling pits were observed on the worn surface of the Ti-10 wt-% Mo alloy, indicating the
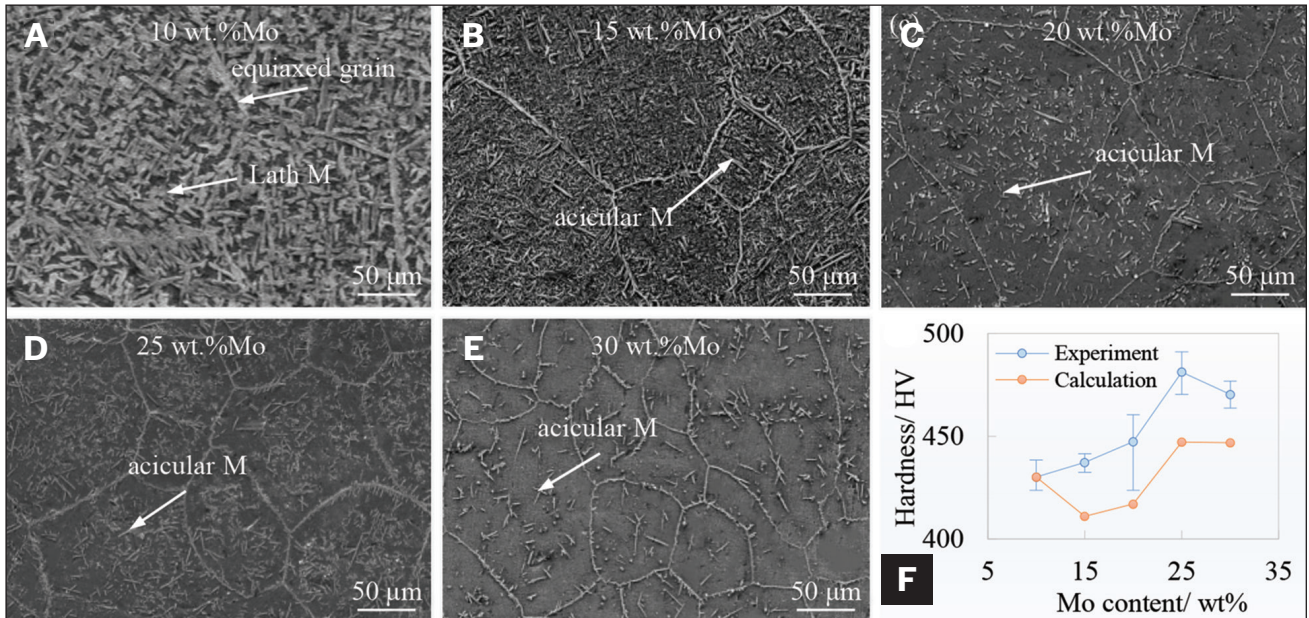
Fig. 3 — SEM images of: A — Ti-10 wt-% Mo alloy; B — Ti-15 wt-% Mo alloy; C — Ti-20 wt-% Mo alloy; D — Ti-25 wt-% Mo alloy; E — Ti-30 wt-% Mo alloy; F — hardnesses of the Ti-x Mo alloys.

adhesive wear behavior was dominant. As shown in Figs. 4C–F, when the Mo contents increased to 15 wt-%, 20 wt-%, and 30 wt-%, the debris became smaller, the peeling pits disappeared, and plowing grooves appeared, which were the characteristics of abrasive wear. When the Mo content was 25 wt-%, the debris disappeared and obvious plowing grooves were observed, indicating the wear mechanism was abrasive wear. The wear performances of the Ti-xMo alloys had a similar trend with the hardness results.

Discussion

Collings et al. (Ref. 19) showed that the ω phase formed at a high Mo content and a high cooling rate in Ti-Mo alloys. Duan et al. (Ref. 20) suggested that in laser powder bed fusion processing of Ti-Mo alloys, a low laser energy density promoted a″ phase formation. In this study, the laser power was high (1.5 kW), and the scanning speed was low (0.3 m [0.984 ft]/min), so the cooling rate was relatively low. The volume fractions of the ω and a″ phases were low and were hard to detect by XRD. The α phase fraction decreased from 68.9% to 7.6% when the Mo content increased from 10 wt-% to 30 wt-%, as shown in Fig. 5A. According to the Ti-Mo equilibrium phase diagram (Ref. 21), the solidification path of the Ti-Mo alloys can be summarized as follows: $L \rightarrow L + \beta \rightarrow \beta \rightarrow \alpha + \beta$. With increasing Mo content, the formation and cohesive energies of the β phase decreased, as presented in Fig. 5B. When the Mo content was 10 wt-%, the cohesive energy of the β phase was –8.27 eV. The cohesive energies of the β phase decreased by 2.6%, 4.9%, 6.7%, and 8.1%, respectively, when the Mo contents increased to 15 wt-%, 20 wt-%, 25 wt-%, and 30 wt-%. It can be concluded that the increasing Mo content enhances the stability of the β phase and inhibits the $\beta \rightarrow \alpha$ phase transformation.

During the solidification of the Ti-Mo alloys, segregation of the Mo element facilitates constitutional undercooling at the solid/liquid interface. Based on the interdependency theory for grain refinement, "secondary" nucleation within the constitutional undercooling zone can restrict the growth of the "primary" grain, resulting in grain refinement (Ref. 22). The grain-refining efficiency of solutes can be quantitatively expressed by the growth restriction factor Q, as calculated by (Ref. 23):

$$Q = mc_0(k - 1) \tag{8}$$

where m is the gradient of the liquidus slope, c_o is the solute concentration in a binary alloy, and k is the partition coefficient.

For the Mo solute, the value of k is about 2.0 (Ref. 23). The average value of m is 6.5°C/wt-%. The calculated Q value increased with increasing Mo content, as did the grain refining efficiency. The maximum Q value was about 195 for Ti-30 wt-% Mo alloy.

The relative grain size (RGS) for binary alloys can be calculated by (Ref. 24):

$$RGS = 1 - \left(\frac{mc_0}{mc_0 - \Delta T_n}\right)^{\frac{1}{1-k}} \tag{9}$$

where ΔT_n is the undercooling required for nucleation, and its value is about 12°C (54°F) for β titanium alloys.
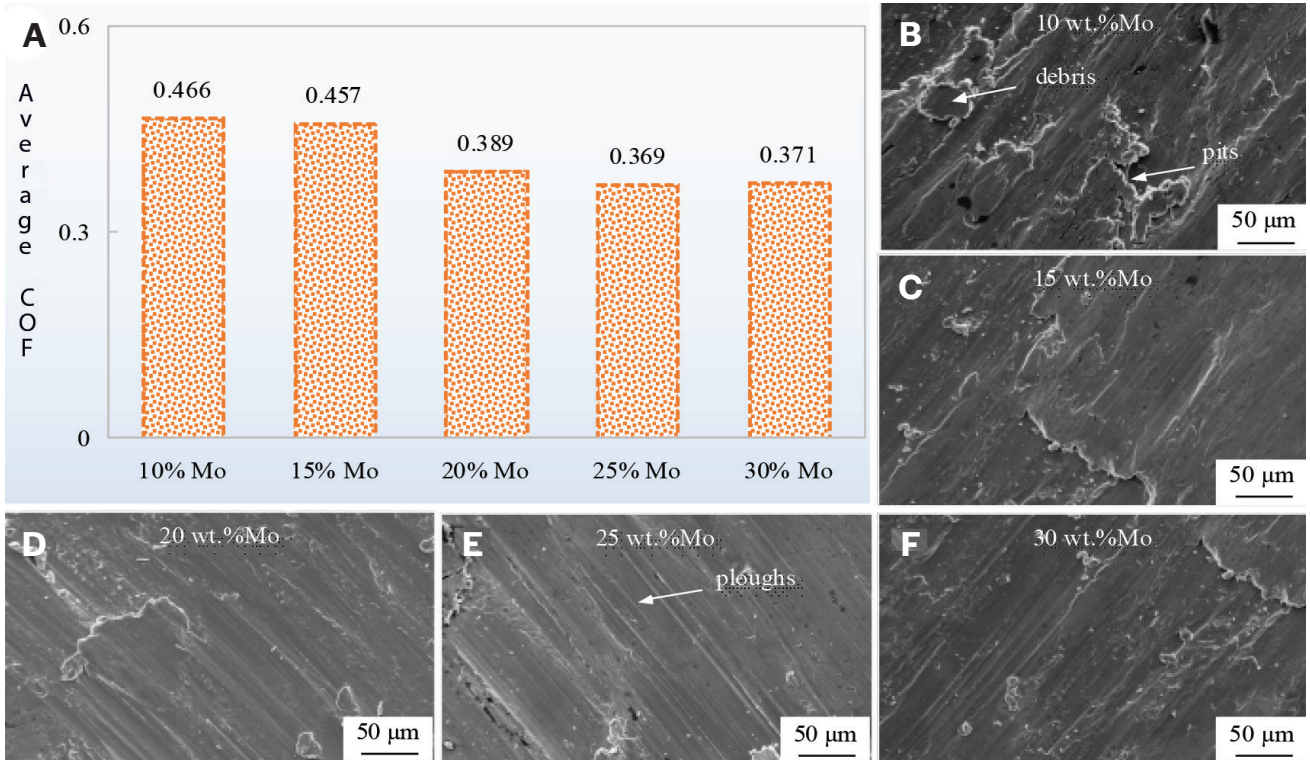
Fig. 4 — A — Average COF. Wear surface morphology of: B — Ti-10 wt-% Mo alloy; C — Ti-15 wt-% Mo alloy; D — Ti-20 wt-% Mo alloy; E — Ti-25 wt-% Mo alloy; F — Ti-30 wt-% Mo alloy.
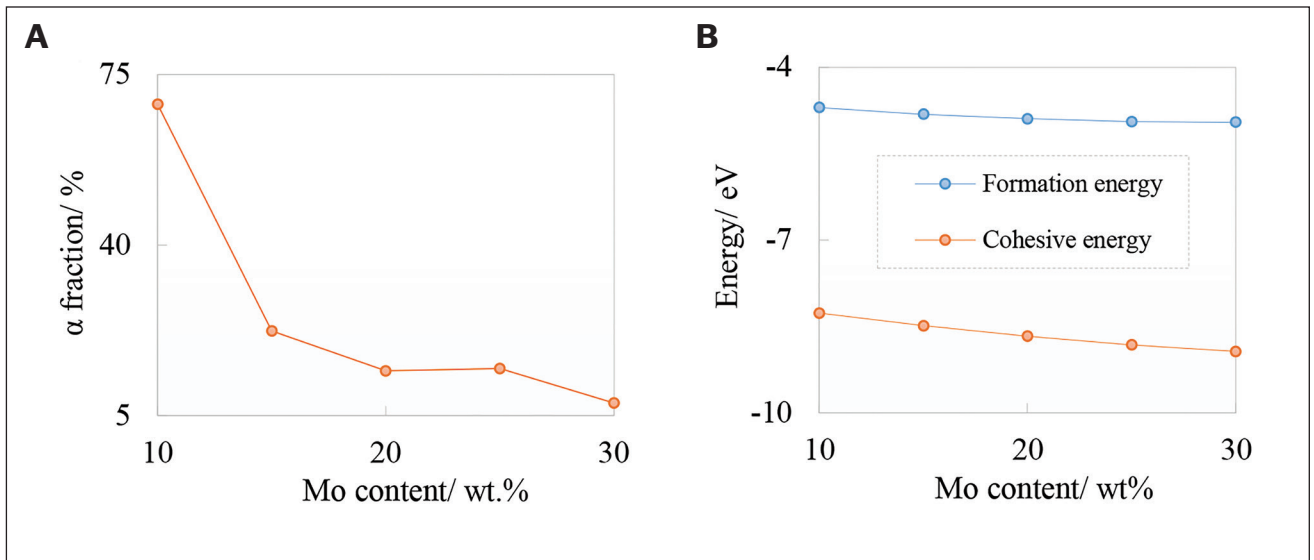

Fig. 5 — A — α phase fraction; B — calculated formation and cohesive energies of the β phase.

The RGS value shows the relative change in grain size with the solute concentration and potency of the nucleant particles. The undercooling remains constant at 12°C for all Ti-xMo alloys. As shown in Fig. 6A, the calculated RGS value decreased with increasing Mo content.

For steel and many other alloy systems, the change from a slipped to a twinned substructure appears to be related to the M_s temperature (Ref. 21). Combining the non-equilibrium

pathway with the specialized Ti-Mo binary phase diagram, which includes the M_s temperature, provides a multidimensional perspective on phase transformation in Ti-Mo alloys. Flower et al. (Ref. 25) and Huang et al. (Ref. 26) reported the M_s temperature of Ti-Mo alloys based on thermal analysis data. As shown in Fig. 6B, the M_s temperature decreases with increasing Mo content. Based on previous studies (Refs. 21, 27), it can be surmised that when the Mo content was
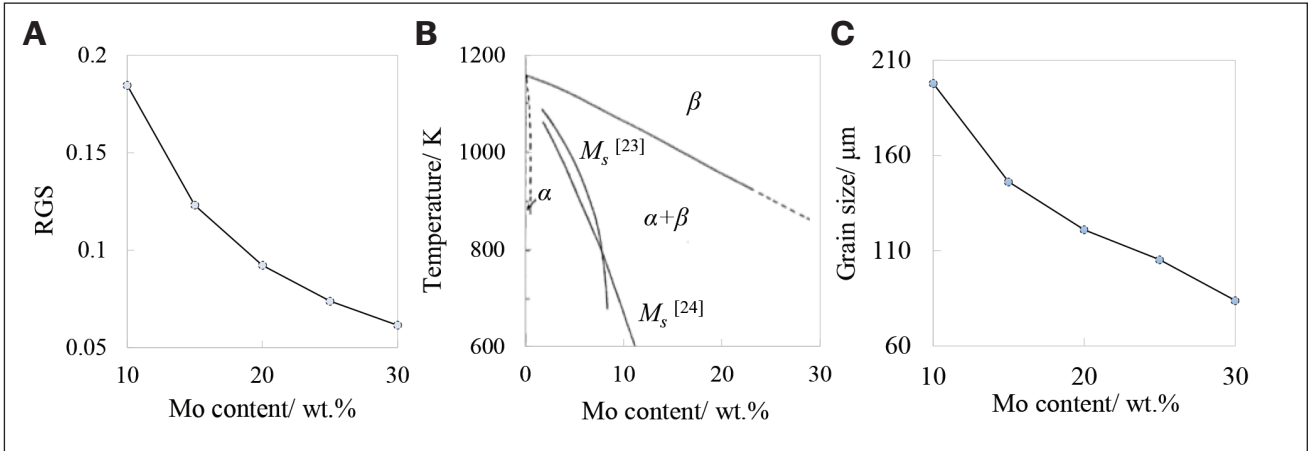
Fig. 6 — A — Calculated RGS value; B — Ti-Mo binary phase diagram; C — grain size.
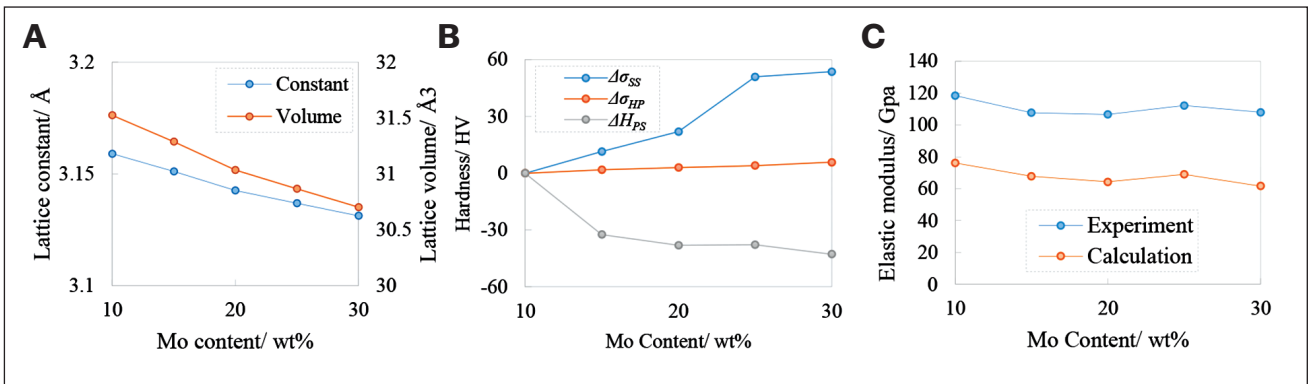

Fig. 7 — A — Calculated lattice constant and volume; B — the contributions of three effects; C — comparisons of the experimental and calculated elastic modulus.

Table 1 — Detailed Values of the Parameters

Parameter	Z	ξ	c	|δ|	η	K / MPa. mm$^{-1/2}$	Hα / GPa	Hβ / GPa
Value	1/550 (Ref. 31)	2.0 (Ref. 28)	16 (Ref. 28)	0.072	2.949	15.7 (Ref. 29)	2.11	1.43

10 wt-%, the M_s temperature was high, and lath martensite formed when slip occurred in the prior β phase. With increasing Mo content, the stability of the β phase and solid solution strengthening effect enhanced, while the M_s temperature decreased. Twins essentially allowed the martensite to accommodate its shape deformation more coherently with the surrounding matrix, reducing the driving force needed for the transformation to proceed. As a result, the slip in the prior β phase was suppressed and the twinning contributed to the lattice invariant shear, causing the acicular martensite formation. In summary, the presence of acicular martensite is a consequence of both the characteristics of the martensitic transformation and the specific influence of the Mo element.

As discussed above, increasing Mo content enhanced the grain refining efficiency and decreased the value of RGS, thereby refining the grain size, as shown in Fig. 6C. The increasing Mo content decreased the M_s temperature and, thus, promoted the acicular martensite formation.

The atom radius of Mo (136 pm) is smaller than that of Ti (145 pm). As a substitution atom, the supersaturated Mo atom decreases the lattice constant and volume of the Ti matrix. The lattice constant (L) and volume of the Ti matrix almost decreased linearly with increasing Mo content, as shown in Fig. 7A. The solid-solution hardening effect ($\Delta_{\sigma SS}$) in binary alloys is due to the variation in the lattice coordinates with respect to ideal positions, which can be calculated by (Ref. 28):

$$\Delta\sigma_{SS} = Ax^{2/3} \qquad (10)$$

where x is the solute concentration, and A can be simplified as:

$$A = 3\mu Z\left(\xi(c^2|\delta|^2 + \eta^2)^{1/2}\right)^{4/3} \qquad (11)$$

where μ is the shear modulus of the alloy, Z is a constant, ξ is a parameter related to the activated slip systems in the different crystal structures, c is a parameter considering the difference in the interaction forces between screw and edge dislocations and the solute atom, δ is the atomic size misfit, and η is the elastic misfit. Values for the constants appear in Table 1.

The grain refinement strengthening effect ($\Delta_{\sigma HP}$) can be described by the Hall-Petch equation (Ref. 29):

$$\Delta\sigma_{HP} = \sigma_y - \sigma_0 = KD^{-1/2} \qquad (12)$$

where σ_y is the yield strength, D is the grain size, and σ_0 and K are experimental constants

The indentation hardness of the α phase is higher than that of the β phase, and the contribution of each phase is evaluated by the product of the hardness of the phase and its fraction (Ref. 30). The hardnesses of the α and β phases were calculated by the first-principal model (Ref. 16), and the α strengthening effect or β phase softening effect (ΔH_{PS}) can be described by:

$$\Delta H_{PS} = H_\alpha \Delta f_\alpha + H_\beta \Delta f_\beta \qquad (13)$$

where H_α and H_β are the hardnesses of the α and β phases, respectively, and Δf_α and Δf_β are the fraction increments of the α and β phases, respectively. The unit of the hardness, Gpa, is converted to Hv (1Gpa = 102.04 Hv).

The values of the parameters for calculating $\Delta_{\sigma SS}$, $\Delta_{\sigma HP}$, and $\Delta_{\sigma PS}$ are summarized in Table 1. The hardness is approximately three times the yield strength. The hardness of the Ti-10 wt-% Mo alloy was adopted as a base value, and the solid-solution hardening effect, grain refinement strengthening effect, and β phase softening effect of other alloys were calculated, as summarized in Fig. 7B. The solid-solution hardening effect had a dominant influence on the hardness increment with increasing Mo content, while the grain refinement strengthening effect had a minor influence owing to the large grain size. When the Mo content increased to 30 wt-%, the β phase softening effect became dominant and decreased the hardness. The calculated hardnesses showed a similar trend as the experimental results, except for the Ti-15 wt-% Mo alloy, whose hardness decreased, as summarized in Fig. 3F. The

deviation between the calculated and experimental results may have been caused by the neglect of α phase morphology in the calculation.

As shown in Fig. 7C, in both the experiment and calculation, the elastic modulus decreased first, then increased, and finally decreased with increasing Mo content. The minimum values of the experimental and calculated elastic modulus were 106.7 Gpa and 64.34 Gpa, respectively. As the α phase had a higher elastic modulus than the β phase and only the β phase was employed in the first-principal model, the experimental values of the elastic modulus were higher than the calculated values.

Conclusions

The laser-directed energy deposition process was employed to fabricate the Ti-Mo alloys with variable Mo contents, and the microstructure and performance were investigated based on experiment and calculation. The following conclusions can be drawn:

1. Increasing Mo content decreases the formation and cohesive energies, thereby stabilizing the β phase.

2. Increasing Mo content increases the grain refining efficiency and decreases the RGS value, thereby refining the grain size.

3. Increasing Mo content decreases the M_s temperature and promotes the acicular martensite formation.

4. Both the solid-solution hardening and fine grain strengthening effects contribute to the increase of the hardness and wear performance, while the β phase softening effect decreases them with increasing Mo content.

Disclosure Statement

No potential conflict of interest was reported by the author.

References

1. Revathi, A., Borrás, A. D., Muñoz, A. I., Richard, C., and Manivasagam, G. 2017. Degradation mechanisms and future challenges of titanium and its alloys for dental implant applications in oral environment. *Materials Science and Engineering: C* 76: 1354–1368. DOI: 10.1016/j.msec.2017.02.159

2. Shi, Q., Yang, S., Sun, Y., Gu, Y., Mercelis, B., Zhong, S., Van Meerbeek, B., and Politis, C. 2022. In-situ formation of Ti-Mo biomaterials by selective laser melting of Ti/Mo and Ti/Mo$_2$C powder mixtures: A comparative study on microstructure, mechanical and wear performance, and thermal mechanisms. *Journal of Materials Science & Technology* 115: 81–96. DOI: 10.1016/j.jmst.2021.09.017

3. Noyama, Y., Miura, T., Ishimoto, T., Itaya, T., Niinomi, M., and Nakano, T. 2012. Bone loss and reduced bone quality of the human femur after total hip arthroplasty under stress-shielding effects by titanium-based implant. *Materials Transactions* 53(3): 565–570. DOI: 10.2320/matertrans.M2011358

4. Cardoso, F. F., Ferrandini, P. L., Lopes, E. S., Cremasco, A., and Caram, R. 2014. Ti–Mo alloys employed as biomaterials: effects of composition and aging heat treatment on microstructure and mechanical behavior. *Journal of the Mechanical Behavior of Biomedical Materials* 32: 31–38. DOI: 10.1016/j.jmbbm.2013.11.021

5. Xie, F., He, X., Cao, S., Mei, M., and Qu, X. 2013. Influence of pore characteristics on microstructure, mechanical properties and corrosion resistance of selective laser sintered porous Ti–Mo alloys for biomedical applications. *Electrochimica Acta* 105: 121–129. DOI: 10.1016/j.electacta.2013.04.105

6. Zhang, W. D., Liu, Y., Wu, H., Song, M., Zhang, T. Y., Lan, X. D., and Yao, T. H. 2015. Elastic modulus of phases in Ti–Mo alloys. *Materials Characterization* 106: 302–307. DOI: 10.1016/j.matchar.2015.06.008

7. Xu, J. L., Tao, S. C., Bao, L. Z., Luo, J. M., and Zheng, Y. F. 2019. Effects of Mo contents on the microstructure, properties and cytocompatibility of the microwave sintered porous Ti-Mo alloys. *Materials Science and Engineering: C* 97: 156–165. DOI: 10.1016/j.msec.2018.12.028

8. Ho, W. F., Ju, C. P., and Lin, J. C. 1999. Structure and properties of cast binary Ti–Mo alloys. *Biomaterials* 20(22): 2115–2122. DOI: 10.1016/S0142-9612(99)00114-3

9. Kang, N., Li, Y., Lin, X., Feng, E., and Huang, W. 2019. Microstructure and tensile properties of Ti-Mo alloys manufactured via using laser powder bed fusion. *Journal of Alloys and Compounds* 771: 877–884. DOI: 10.1016/j.jallcom.2018.09.008

10. Kang, N., Lin, X., El Mansori, M., Wang, Q. Z., Lu, J. L., Coddet, C., and Huang, W. D. 2020. On the effect of the thermal cycle during the directed energy deposition application to the in-situ production of a Ti-Mo alloy functionally graded structure. *Additive Manufacturing* 31: 100911. DOI: 10.1016/j.addma.2019.100911

11. Hossein, N. S., Yildiz, M., and Saboori, A. 2022. Solidification behaviour of austenitic stainless steels during welding and directed energy deposition. *Science and Technology of Welding and Joining* 28: 1–17. DOI: 10.1080/13621718.2022.2115664

12. Marker, C., Shang, S. L., Zhao, J. C., and Liu, Z. K. 2018. Effects of alloying elements on the elastic properties of bcc Ti-X alloys from first-principles calculations. *Computational Materials Science* 142: 215–226. DOI: 10.1016/j.commatsci.2017.10.016

13. You, L., and Song, X. 2012. First principles study of low Young's modulus Ti–Nb–Zr alloy system. *Materials Letters* 80: 165–167. DOI: 10.1016/j.matlet.2012.01.145

14. Xi, Z., Sen, Y., Jiming, Z., Hanyuan, L., Jun, C., and Xiqun, M. 2021. First-Principles Calculation of Low Young's Modulus Ti-Mo-Sn Alloys for Biomedical Applications. *Rare Metal Materials and Engineering* 50(1): 35–42.

15. Ikehata, H., Nagasako, N., Furuta, T., Fukumoto, A., Miwa, K., and Saito, T. 2004. First-principles calculations for development of low elastic modulus Ti alloys. *Physical Review B* 70(17): 174113. DOI: 10.1103/PhysRevB.70.174113

16. Miao, N., Sa, B., Zhou, J., and Sun, Z. 2011. Theoretical investigation on the transition-metal borides with Ta_3B_4-type structure: A class of hard and refractory materials. *Computational Materials Science* 50(4): 1559–1566. DOI: 10.1016/j.commatsci.2010.12.015

17. Luke, C.A., Taggart, R., and Polonis, D.H. 1965. Electronic factors and the metastable constitution of quenched alloys based on titanium and zirconium. *Journal of Nuclear Materials* 16(1): 7–18. DOI: 10.1016/0022-3115(65)90086-3

18. Rastogi, A., Sarkar, R., and Neelakantan, S. 2023. Transitions among martensitic phases during continuous deformation in metastable β Ti-10V-2Fe-3Al alloy. *Journal of Alloys and Compounds* 964: 171320. DOI: 10.1016/j.jallcom.2023.171320

19. Collings, E. W., and Ho, J. C. 1976. Solute-induced lattice stability as it relates to superconductivity in titanium-molybdenum alloys. *Solid State Communications* 18: 1493–1495. DOI: 10.1016/0038-1098(76)90377-X

20. Duan, R., Li, S., Cai, B., Tao, Z., Zhu, W., Ren, F., and Attallah, M. M. 2021. In situ alloying based laser powder bed fusion processing of β Ti–Mo alloy to fabricate functionally graded composites. *Composites Part B: Engineering* 222: 109059. DOI: 10.1016/j.compositesb.2021.109059

21. Davis, R., Flower, H. M., and West, D. R. F. 1979. Martensitic transformations in Ti-Mo alloys. *Journal of Materials Science* 14: 712–722. DOI: 10.1007/BF00772735

22. StJohn, D. H., Qian, M., Easton, M. A., and Cao, P. 2011. The Interdependence Theory: The relationship between grain formation and nucleant selection. *Acta Materialia* 59(12): 4907–4921. DOI: 10.1016/j.actamat.2011.04.035

23. Bermingham, M. J., McDonald, S. D., Dargusch, M. S., and StJohn, D. H. 2008. Grain-refinement mechanisms in titanium alloys. *Journal of Materials Research* 23(1): 97–104. DOI: 10.1557/JMR.2008.0002

24. Easton, M. A. and StJohn, D. H. 2001. A model of grain refinement incorporating alloy constitution and potency of heterogeneous nucleant particles. *Acta Materialia* 49(10): 1867–1878. DOI: 10.1016/S1359-6454(00)00368-2

25. Flower, H. M., Henry, S. D., and West, D. R. F. 1974. The β-α transformation in dilute Ti–Mo alloys. *Journal of Materials Science* 9: 57–64. DOI:10.1007/BF00554755

26. Huang, Y. C., Suzuki, S., Kaneko, H., and Sato, T. 1970. *The Science, Technology and Application of Titanium*. Pergamon Press 691–695.

27. Flower, H. M., Swann, P. R., and West, D. R. F. 1972. The effect of Si, Zr, Al and Mo on the structure and strength of Ti martensite. *Journal of Materials Science* 7: 929–938. DOI:10.1007/BF00550440

28. Caraballo, I. T. 2017. A general formulation for solid solution hardening effect in multicomponent alloys. *Scripta Materialia* 127: 113–117. DOI: 10.1016/j.scriptamat.2016.09.009

29. Issariyapat, A., Visuttipitukul, P., Umeda, J., and Kondoh, K. 2020. Refined grain formation behavior and strengthening mechanism of α-titanium with nitrogen fabricated by selective laser melting. *Additive Manufacturing* 36: 101537. DOI: 10.1016/j.addma.2020.101537

30. Liu, Z., and Welsch, G. 1988. Effects of oxygen and heat treatment on the mechanical properties of alpha and beta titanium alloys. *Metallurgical Transactions A* 19: 527–542. DOI: 10.1007/BF02649267

31. Kou, H., Li, W., Ma, J., Shao, J., Tao, Y., Zhang, X., Geng, P., Deng, Y., Li, Y., Zhang, X., and Peng, F. 2018. Theoretical prediction of the temperature-dependent yield strength of solid solution strengthening Nickel-based alloys. *International Journal of Mechanical Sciences* 140: 83–92. DOI: 10.1016/j.ijmecsci.2018.02.042

DA SHU and **LEI ZHAO** are with the School of Mechanical Engineering, Anhui Polytechnic University, Wuhu, People's Republic of China. **SHU** is also with the Nano and Molecular Systems Research Unit, Faculty of Science, University of Oulu, Finland. **DONGSHENG WU** (*d.wu@jwri.osaka-u.ac.jp*) and **NINSHU MA** are with the Joining and Welding Research Institute (JWRI), Osaka University, Osaka, Japan. **YANBING GUO** is with the College of Ocean Science and Engineering, Institute of Marine Materials Science and Engineering, Shanghai Maritime University, Shanghai, China. **ZHIXI ZHANG** is with the School of Materials Engineering, Shanghai Dianji University, Shanghai, China.